



Swansea University  
Prifysgol Abertawe



## Cronfa - Swansea University Open Access Repository

---

This is an author produced version of a paper published in:

*Fusion Engineering and Design*

Cronfa URL for this paper:

<http://cronfa.swan.ac.uk/Record/cronfa39529>

---

### **Paper:**

Evans, L., Margetts, L., Casalegno, V., Leonard, F., Lowe, T., Lee, P., Schmidt, M. & Mummery, P. (2014). Thermal characterisation of ceramic/metal joining techniques for fusion applications using X-ray tomography. *Fusion Engineering and Design*, 89(6), 826-836.

<http://dx.doi.org/10.1016/j.fusengdes.2014.05.002>

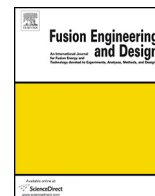
---

This item is brought to you by Swansea University. Any person downloading material is agreeing to abide by the terms of the repository licence. Copies of full text items may be used or reproduced in any format or medium, without prior permission for personal research or study, educational or non-commercial purposes only. The copyright for any work remains with the original author unless otherwise specified. The full-text must not be sold in any format or medium without the formal permission of the copyright holder.

Permission for multiple reproductions should be obtained from the original author.

Authors are personally responsible for adhering to copyright and publisher restrictions when uploading content to the repository.

<http://www.swansea.ac.uk/library/researchsupport/ris-support/>



# Thermal characterisation of ceramic/metal joining techniques for fusion applications using X-ray tomography

LI.M. Evans<sup>a,\*</sup>, L. Margetts<sup>b</sup>, V. Casalegno<sup>c</sup>, F. Leonard<sup>a</sup>, T. Lowe<sup>a</sup>, P.D. Lee<sup>a</sup>, M. Schmidt<sup>d</sup>, P.M. Mummery<sup>d</sup>

<sup>a</sup> School of Materials, University of Manchester, Grosvenor Street, Manchester M1 7HS, UK

<sup>b</sup> School of Earth, Atmospheric and Environmental Sciences, University of Manchester, Williamson Building, Manchester M13 9PL, UK

<sup>c</sup> Department of Applied Science and Technology, Politecnico di Torino, Corso Duca degli Abruzzi 24, I-10129 Torino, Italy

<sup>d</sup> School of Mechanical, Aerospace and Civil Engineering (MACE), University of Manchester, Manchester M13 9PL, UK

## ARTICLE INFO

### Article history:

Received 9 December 2013

Received in revised form 25 April 2014

Accepted 5 May 2014

Available online 5 June 2014

### Keywords:

Thermal conductivity  
Laser flash  
X-ray tomography  
Carbon fibre composites  
Copper  
Joining

## ABSTRACT

This work investigates the thermal performance of four novel CFC–Cu joining techniques. Two involve direct casting and brazing of Cu onto a chromium modified CFC surface, the other two pre-coat a brazing alloy with chromium using galvanisation and sputtering processes. The chromium carbide layer at the interface has been shown to improve adhesion. Thermal conductivity across the join interface was measured by laser flash analysis. X-ray tomography was performed to investigate micro-structures that might influence the thermal behaviour. It was found that thermal conductivity varied by up to 72%. Quantification of the X-ray tomography data showed that the dominant feature in reducing thermal conductivity was the lateral spread of voids at the interface. Correlations were made to estimate the extent of this effect.

© 2014 The Authors. Published by Elsevier B.V. This is an open access article under the CC BY license (<http://creativecommons.org/licenses/by/3.0/>).

## 1. Introduction

ITER, the next step on the world's pathway to realising fusion energy, aims to demonstrate the feasibility of using fusion reactions to drive a power plant by successfully sustaining a controlled large scale plasma burn. As well as controlling the plasma, it must show that the construction materials will withstand the thermo-mechanical loading caused by the plasma and any disruptions experienced [1]. As such, the main role of the divertor plasma facing components (PFC) is to protect the machine from this loading by absorbing the energy released whilst minimising plasma impurities and retaining structural integrity [2]. ITER's design specifications will achieve this by active water cooling of the PFCs through heat sinks made from copper chromium zirconium (CuCrZr), a precipitation hardened copper alloy. Thus, the ability to join the PFCs to the CuCrZr is essential [3,4].

The divertor PFCs, which are the target at the intersection of magnetic field lines carrying the plasma, are expected to experience the highest loads, around  $10 \text{ MW m}^{-2}$ , as the kinetic energy

is dumped over this region [5]. Under certain modes of operation these loads could exceed  $10 \text{ MW m}^{-2}$ , but this is not expected under normal in-service conditions. Materials selected for this component will be required to have high thermal conductivity and high thermal shock and fatigue resistance without impacting plasma purity. The two materials under consideration that meet these requirements are carbon fibre composites (CFC) and tungsten [6]. ITER was originally designed to have a two tier divertor, using both materials, with the CFC being replaced by tungsten at a later phase of ITER's lifecycle. As a cost reduction measure it was decided to use an all-tungsten divertor, however CFC components which require joining may be used elsewhere and in future fusion reactor designs [7].

The CFC region of the divertor consisted of rows of monoblocks along the cooling pipes. This design was chosen because other candidates, such as flat tiles or saddleblocks, suffered rapid and complete debonding [2,8]. The monoblock is a CFC cuboid with a cylindrical hole in the centre through which a CuCrZr coolant pipe runs, as shown in Fig. 1. The region between the two is the interface that requires joining. A large difference in the coefficient of thermal expansion of the two materials causes large internal stresses during operation, which can lead to failure. It has been suggested that a thin Cu interlayer might be used in order to mitigate these

\* Corresponding author. Tel.: +44 1235 466524.

E-mail address: [lion.evans@ccfe.ac.uk](mailto:lion.evans@ccfe.ac.uk) (LI.M. Evans).

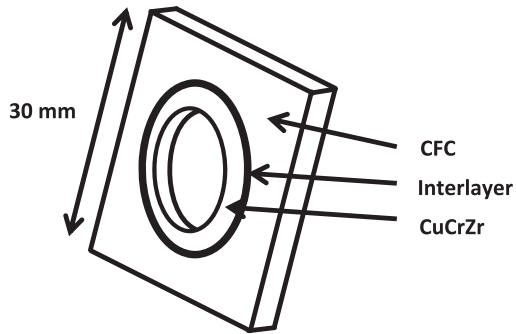


Fig. 1. Schematic of divertor monoblock.

stresses through its superior ductility. However, CFC does not bond well with pure Cu [9] since the wetting angle of molten copper on carbon substrates is very high, approximately  $140^\circ$ .

A wide range of techniques have been suggested to overcome this challenge [10–15]. This work investigates the thermal behaviour of four CFC–Cu joining methods, developed by Casalegno et al. [9,16,17], which involve introducing a thin layer of chromium carbide to improve adhesion. Thermal performance across the interfaces is investigated experimentally using laser flash analysis (LFA). The sample interfaces are then investigated by X-ray tomography. Particular interest is given to microstructural variations to identify mechanisms responsible for differences in thermal conductivity. The aim of this investigation is to determine which joining technique provides the greatest thermal conductivity across the CFC–Cu interface and which observable microstructures introduced in the joining process can impede thermal conductivity.

## 2. Materials

In order to create specimens suitable for thermal testing, tiles were manufactured in such a way as to represent the CFC–Cu interface present in the monoblock. Each tile consisted of a layer of

CFC and Cu, with the interface created by one of the four differing methods of joining.

Two of these used a CFC where the interface surface is modified to form carbides by a solid state chemical reaction with chromium, which has been shown to improve wettability of Cu with CFC [18]. One sample (CFC–Cu\_DC) was joined by a direct casting of a Cu slurry to the modified CFC by placing both materials adjacently in a holder and being heated to  $1100^\circ\text{C}$  for 20 min. The other (CFC–Cu\_OSB) was brazed using a commercial brazing alloy containing no active metals, where the tile is heated to  $980^\circ\text{C}$  in an inert argon atmosphere and is kept at this maximum temperature for 15 min before being allowed to cool to room temperature. Adhesion between the two layers was facilitated by the use of a tungsten weight on the upper surface of the tile, exerting 1 kPa of pressure.

In a similar vein, the final two samples were brazed using the same brazing alloy and procedure but the chromium was pre-coated to the brazing foil rather than the CFC. This was achieved by a galvanic process (CFC–Cu\_GG) and RF magnetron sputtering (CFC–Cu\_GS). Coating the foil with chromium on a large scale would be technically less challenging than modifying the CFC surface of a monoblock and would therefore be a more cost-effective manufacturing process. The joining processes were performed at Politecnico di Torino according to the procedures detailed by Casalegno et al. [17].

The CFC used was Sepcarb NB31 (Snecca Propulsion Solid, France). The composite is composed of a 3D NOVOLTEX preform with needled ex-pitch (z-direction) and ex-PAN (x and y directions) fibres. Densification is performed by chemical vapour infiltration (CVI). The copper was an oxygen free high conductivity (OFHC) variety and the unmodified brazing foil was Gemco<sup>®</sup> (87.75 wt% Cu, 12 wt% Ge and 0.25 wt% Ni), both manufactured by Wesgo Metals, USA.

Further preparation, undertaken at The University of Manchester, was made to machine the tiles to appropriate dimensions for thermal analysis. This was achieved by using a lathe to produce cylindrical samples, except for the CFC–Cu\_DC sample which was cored out of the tile using the appropriate drill bit. A sample thickness suitable for analysis was achieved using an aluminium oxide

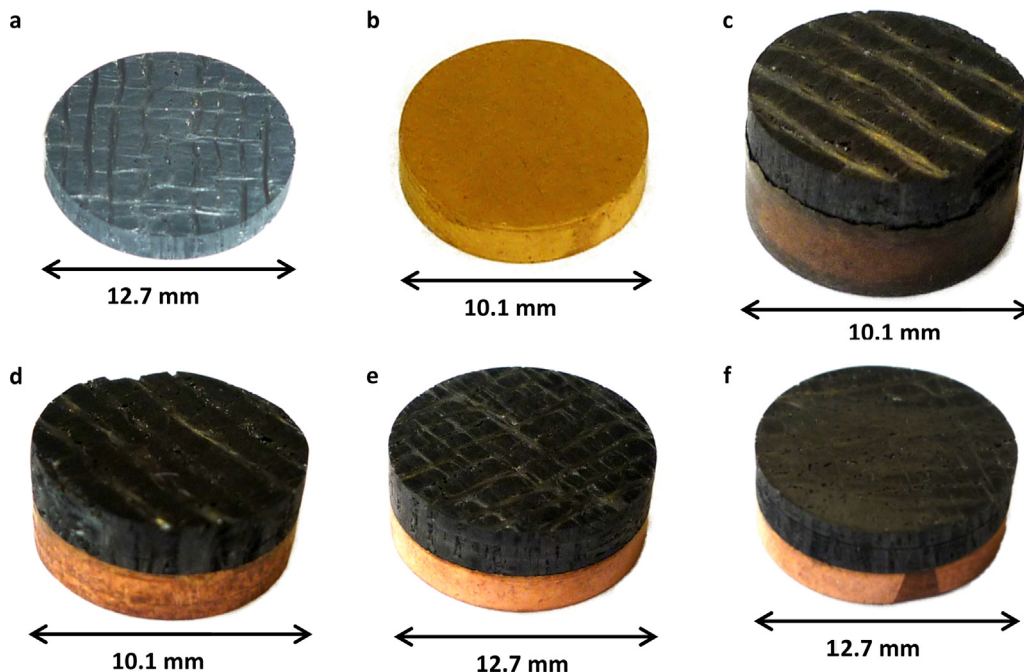


Fig. 2. Samples used for thermal analysis; (a) CFC, (b) Cu, (c) CFC–Cu joined by; direct casting (DC), (d) one step brazing (OSB), (e) braze coated by galvanisation process (GG), (f) braze coated by sputtering process (GS).

**Table 1**  
Sample dimensions.

Sample	Diameter (mm)	Thickness (mm)	Thickness (%)		Mass ( $\times 10^{-3}$ kg)	Volume ( $\times 10^{-6}$ m <sup>3</sup> )	Density ( $\times 10^3$ kg m <sup>-3</sup> )
			Cu	CFC			
CFC	12.66	2.06			0.447	0.2593	1.72
Cu	10.10	2.06			1.421	0.1650	8.61
CFC–Cu_DC	10.08	5.36	48.7	51.3	2.191	0.4277	5.12
CFC–Cu.OSB	10.08	4.40	46.8	53.2	1.752	0.3511	4.99
CFC–Cu.GG	12.66	4.96	43.5	56.5	2.978	0.6244	4.77
CFC–Cu.GS	12.70	4.84	43.4	56.6	2.916	0.6131	4.76

cutting wheel on a Struers Accutom-5 cut-off machine at 3000 rpm using a medium force at a speed of  $2 \times 10^{-5}$  m·s<sup>-1</sup>. Where required sample grinding using P800 SiC emery paper was performed to obtain parallel upper and lower surfaces. Finally, the samples were cleaned in acetone using an ultrasonic bath for 10 min. Photographic images of the samples can be seen in Fig. 2. Details of the samples' final dimensions and properties can be found in Table 1. The cylindrical volumes were calculated using the samples' diameter and thickness, density was calculated using these values with their mass. As such, data for volume and density are bulk values inclusive of the porosity existing in the CFC. The variation in density due to the different phases is therefore not taken into account. In addition to these were samples for each of the constituent materials (i.e. CFC and Cu) to obtain their individual material properties.

### 3. Method

This section details the experimental setup used to perform thermal analysis and three dimensional imaging. Details are also provided for image post-processing techniques.

#### 3.1. Thermal analysis

LFA was performed using a Netzsch 457 MicroFlash® system [19] at the School of MACE, University of Manchester, UK. This method measures thermal diffusivity,  $k$ , by subjecting the front face of a disc shaped sample to a short duration heat pulse, produced by a Nd:YAG laser, whilst measuring the temperature rise with respect to time on the rear face (see Fig. 3). The half rise time,  $t_{1/2}$ , along with sample thickness,  $L$ , and correction factor,  $\omega$ , are used by the 'Cowan + pulse correction' method [20], a modified version of the Parker expression [21] to account for finite-pulse-time and heat losses (1), to determine the sample's thermal diffusivity. Specific heat,  $c_p$ , is measured by calibrating diffusivity results against a Pyroceram 9606 reference sample. Thermal conductivity,  $K$ , can be calculated from its relation to these values and density,

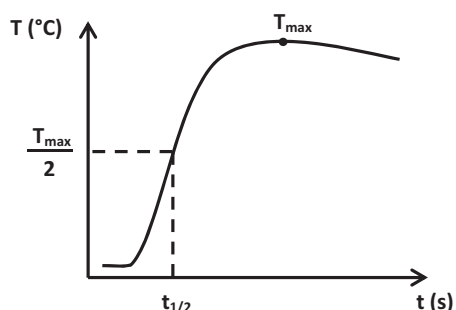


**Fig. 3.** Typical temperature curve measured on rear face of sample after initial heat pulse.

$\rho$ , (2) whose temperature dependant values are obtained from the thermal expansion coefficient.

$$\kappa = \frac{\omega \cdot L^2}{\pi^2 \cdot t_{1/2}} \quad (1)$$

$$K = \rho \cdot c_p \cdot \kappa \quad (2)$$

The measurements were conducted in an inert nitrogen atmosphere at temperatures ranging from 100 °C to 700 °C at intervals of approximately 100 °C. This range includes the expected working temperature of the component's joined region, where coolant inlet temperature will be around 150 °C. Because of the relatively high thermal conductivity of the samples the laser voltage was set to its minimum setting. An average value was obtained from 5 measurements at each temperature. The Proteus software package, version 5.2.1 (NETZSCH-Gerätebau GmbH, Wittelsbacherstraße, Selb, Germany), was used to control the measurements and analyse results. Additional parameters specified were to use a linear baseline, 100% laser filter transmission, 3000 signal acquisition points and to auto optimise amplifier gain and measurement duration.

To ensure maximum absorption of the laser energy and emission on the rear face, the samples were given a conductive graphite coating (Kontakt-Chemie Graphit 33). Multiple coatings are applied to both surfaces, allowing time to dry between applications. Due to the highly anisotropic behaviour of CFCs, it was ensured that fibres in both CFC and CFC–Cu samples were aligned identically to the expected setup of the divertor monoblock [22]. The CFC–Cu samples were tested in both orientations (i.e. laser incident on CFC then Cu), the variation in results was less than 3% and can be considered negligible. Results reported here are with the laser incident on the Cu surface and temperature measured on the CFC surface.

#### 3.2. X-ray tomography

X-ray tomography scans of the samples were produced using a Nikon Metrology 225/320 kV system (using the 225 kV source) at the Manchester X-ray Imaging Facility, University of Manchester, UK. The samples were placed on a rotating stage between the X-ray source and detector. 2D radiographs are acquired whilst the sample is rotated through 360°. 3D reconstruction is performed from the radiographs, to be exported as an individual 3D image or a collection of 2D 'slices'.

The sample specific settings for X-ray source voltage and current, radiograph acquisition time and information about filters used are presented in Table 2. The CT-Pro (Nikon Metrology NV, Tring, Hertfordshire, UK) software was used for tomographic reconstruction. Details for beam hardening and noise reduction settings are noted in Table 3. Resultant voxel sizes (3D pixel), which are dependent on distances between source, sample and detector, are also reported.

#### 3.3. Visualisation and analysis of X-ray tomography data

Each two dimensional slice forming the complete volume is a greyscale image, with higher greyscale values denoting a greater

**Table 2**  
X-ray tomography parameters used.

Sample	Target	Voltage (kV)	Current (μA)	Filter (mm)	Acquisition time (s)	Number of projections	Frames/projection
CFC	Cu	120	200	N/A	0.5	2001	1
Cu	W	220	210	Sn, 1.0	0.7	3142	1
CFC–Cu_DC	W	210	135	Sn, 1.0	1.415	2001	2
CFC–Cu.OSB	W	210	135	Sn, 1.0	1.415	3142	2
CFC–Cu.GG	W	210	135	Sn, 1.0	1.415	2001	2
CFC–Cu.GS	W	210	135	Sn, 1.0	1.415	2001	2

**Table 3**  
Reconstruction settings.

Sample	Beam hardening	Noise reduction	Voxel width (×10 <sup>-6</sup> m)
CFC	1	3	10.0
Cu	2	2	8.2
CFC–Cu_DC	2	4	8.3
CFC–Cu.OSB	2	4	8.3
CFC–Cu.GG	2	4	9.7
CFC–Cu.GS	2	4	9.7

level of X-ray absorption. In order to visualise the sample in three dimensions the greyscale data must first be segmented, a process which assigns a material type to each voxel (3D pixel). Segmentation and visualisation were performed using a combination of the software packages Avizo, version 7 (VSG, Mérignac Cedex, France) and Simpleware, version 6 (Simpleware Ltd., Exeter, Devon, UK). This process also allows the collection of quantitative data about the sample, such as porosity fractions, volumes or surface area of each material and can be used to measure lengths of internal features e.g. cracks.

**4. Results and discussion**

Results are firstly presented on the thermal behaviour of the samples, comparing the performance variations caused by the differing joining techniques. These are benchmarked against the results for the constituent materials and the material property values reported in the ITER materials property handbook (IMPH) [23]. The outcome of the scanning process is then discussed, making particular note of any features likely to affect overall image quality due to sample geometry or material composition. The computed tomography (CT) data is then visualised for investigation of the CFC–Cu interface by both qualitative and quantitative methods. Finally conclusions are drawn based on these observations as to the cause of the thermal performance variations and which joining technique provides the best performance.

**4.1. Thermal diffusivity**

The thermal properties of six samples (CFC, Cu and four joined variants) were measured experimentally. The results for diffusivity, specific heat and conductivity are shown in Figs. 4–6. It is difficult

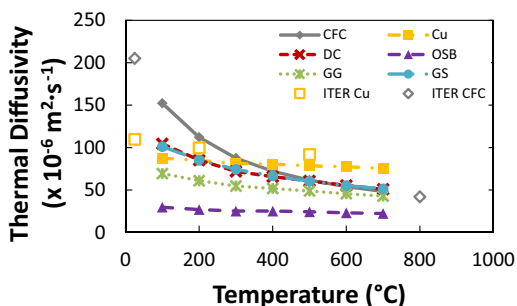


**Fig. 4.** Thermal diffusivity measured by laser flash analysis.

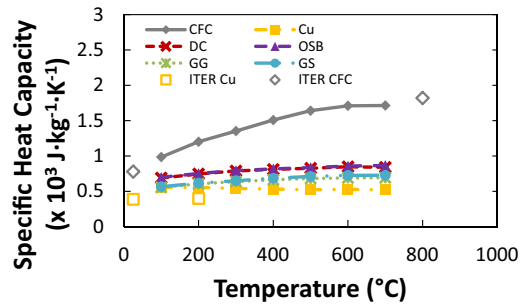


**Fig. 5.** Specific heat capacity calculated by calibration of diffusivity against Pyroceram 9606.

to directly compare the results of the joined samples with each other because each has a different ratio of CFC to Cu thickness. In order to compare results, the average values were calculated for each sample as expected based on the thickness fraction, *R*, of each constituent material, shown in Table 1. The difference,  $\delta$ , between experimental and expected average values for each thermal property are shown in Figs. 7–9, e.g. for thermal diffusivity;

$$\delta_{\kappa} = \frac{\kappa_{avg} - \kappa_{exp}}{\kappa_{avg}} \tag{3}$$

$$\kappa_{avg} = \kappa_{CFC} \cdot R_{CFC} + \kappa_{Cu} \cdot R_{Cu} \tag{4}$$

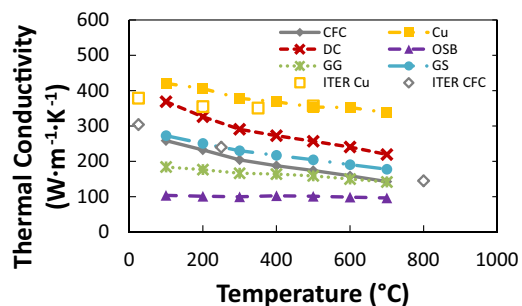


**Fig. 6.** Thermal conductivity calculated from diffusivity, density and specific heat values.

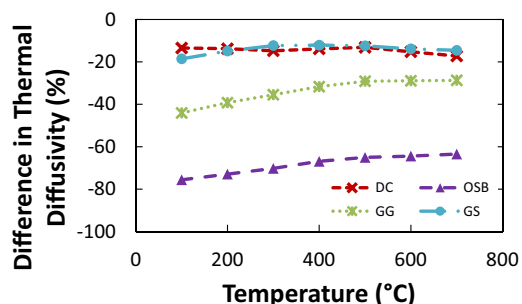


**Fig. 7.** Difference, as a percentage, in sample thermal diffusivity compared to expected value as calculated from constituent material thicknesses.

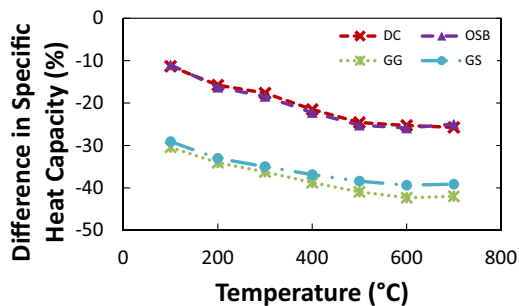


Fig. 8. Difference, as a percentage, in sample specific heat capacity compared to expected value as calculated from constituent material thicknesses.

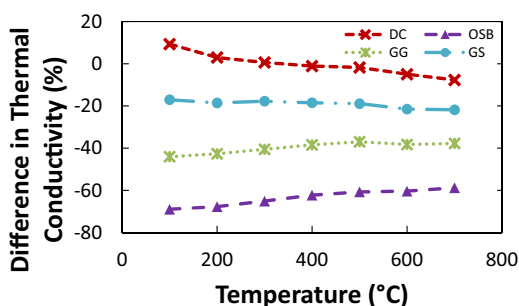


Fig. 9. Difference, as a percentage, in sample thermal conductivity compared to expected value as calculated from constituent material thicknesses.

Firstly it is pertinent to compare the individual results for CFC and Cu to the reference values provided in the IMPH, shown for specific heat and thermal conductivity in Figs. 5 and 6 and Table 4. The thermal diffusivity values shown in Fig. 4 have been calculated from the aforementioned values. It can be seen that the thermal conductivities were slightly lower for CFC and higher for Cu, although these are still within acceptable limits. The experimental results show that Cu is relatively stable over the range of temperatures, with only thermal conductivity experiencing an appreciable drop of approximately 20% of its initial value. The change in temperature has a greater effect on the performance of CFC, with thermal conductivity reducing by 45% over the 600 °C range measured. In all of the joined samples it would therefore be expected to observe similar trends in thermal properties. This is indeed what can be seen although to differing degrees of magnitude.

Comparison of the differences, relative to averages based on material thickness fractions, grants further insight into the influence each bonding technique has on the thermal behaviour. It can be seen (Fig. 9) that the differences in thermal conductivity for the four techniques are very distinct from each other. As the differences do not vary much across the temperature range, approximately 20% for DC and 10% for the others, their tendency is to follow the

Table 4

Materials properties of CFC and Cu as specified by IMPH.

Properties	T (°C)	CFC (z direction)	Cu
Thermal conductivity ( $\text{W m}^{-1} \text{K}^{-1}$ )	RT <sup>a</sup>	304	379
	250/200	240	355
	800/350	145	351
	1000/500	141	357
Specific Heat ( $\times 10^3 \text{ J kg}^{-1} \text{ K}^{-1}$ )	RT	0.780	0.388
	800/200	1.820	0.400
	1000/500	2.000	0.437
	800/200	0.4	17.0
CTE ( $\times 10^{-6} \text{ K}^{-1}$ )	1000/500	0.5	18.6
	RT	1.90	8.90
Density ( $\times 10^3 \text{ kg m}^{-3}$ )	RT	8	N/A
Porosity (%)	RT	8	N/A

<sup>a</sup> Room temperature.

conductivity of the average. That is, the effect of joining on thermal conductivity is relatively consistent across the temperatures investigated.

Interestingly, the samples' specific heat fell into two clear bands. The samples whose specific heat are higher, closer to CFC and change the least are the ones which have the modified CFC surface (DC and OSB). Whereas the samples joined by a modified braze (GG and GS) have lower values more similar to Cu. Even though the diffusivity of DC and GS samples are similar, it is this significant difference in specific heat which causes the DC sample to have an overall higher thermal conductivity.

The expectation is that the thermal conductivities of the joined samples would not be greater than the average values derived from constituent material thicknesses but would be between those. Other than DC performing a little better than the average at low temperatures, the first statement holds true, showing that the four joining techniques do reduce the conductivity. However for OSB and GG samples the conductivity is affected to such an extent that it is lower than that of only CFC.

The joining techniques' effectiveness of carrying thermal energy away is ranked, from low to high, as OSB, GG, GS and DC.

#### 4.2. X-ray tomography

Samples with high X-ray absorption contrasts, such as that between CFCs and Cu, are notoriously difficult to image well [24]. If there is too much X-ray penetration of a region it will appear 'washed-out' and be difficult to distinguish from the surrounding air. Conversely, if penetration is insufficient internal features are very difficult to resolve and large 'streaking' artefacts will be observed emanating from the edges of this region. In consideration of this, careful selection of filters and source energy was made (shown in Table 2) to mitigate these effects which are likely to be more pronounced at the interface where contrast is greatest. It can be seen in Fig. 10 that these effects are not completely suppressed; in the combined image the interface is ill-defined with streaking

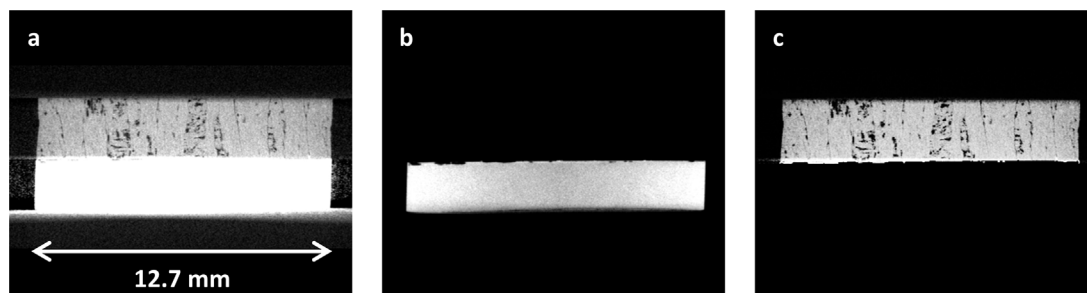
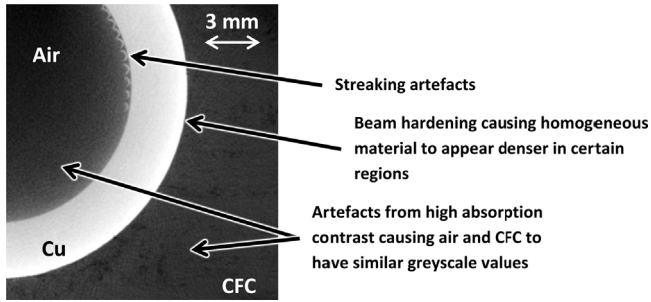


Fig. 10. Cross sectional tomography slice showing (a) streaking artefacts from high absorption Cu masking internal CFC structures at interface, resolved by individually adjusting image brightness and contrast values for (b) Cu and (c) CFC.



**Fig. 11.** Various artefacts that hinder automated segmentation of CT image caused by high absorption contrast ratio in an X-ray tomography slice from the midplane of a CFC–Cu divertor monoblock.

artefacts from the Cu overlapping the CFC. With an appropriate balance of image contrast and brightness levels individual images can be produced that provide enough detail to distinguish between the various materials at the interface. Further artefacts that hinder the process of automated segmentation are displayed in Fig. 11, these must typically be dealt with manually. In this instance, such artefacts were removed using paint/un-paint tools on a slice-by-slice basis by eye to discern material boundaries, using similar structures in the surrounding region for guidance.

#### 4.3. Visualisation and analysis of X-ray tomography data

The porosity contained within the CFC is a good example of where qualitative and quantitative observations can be complementary. Fig. 12(a) shows the full volume of the CFC–Cu\_GS sample. Having distinguished the CFC and Cu phases it is possible to determine the location of the porosity. By digitally removing the CFC it is then possible to see the alignment of the porosity with fibre direction, the thickness of the layers and additional features such as size, shape and distribution of closed or open porosity. By measuring the volume of the CFC and porosity it was possible to measure the volume fraction of the porosity to be 7.5%. By comparison with the IMPH, where porosity fraction is reported as 8%, this can be seen to be in agreement. Across the range of samples, the porosity varied little as all samples used the same manufactured CFC. Therefore, analysis of the CT data concentrates on the CFC–Cu interface, more specifically the differences in how the Cu/braze deforms to bond with the CFC, dependent on joining technique. Although the Cr layer will have some effect on the interface, its thickness is similar to that of the image resolution and therefore will not be discernible.

Two notable features, seen in Fig. 13, were apparent in the DC sample. Firstly, the perimeter of the CFC is surrounded by a thin layer of Cu. The Cu seems to be pulled from the main Cu layer over the CFC layer. This was most probably caused by the process of boring the sample out of a larger tile, the only sample not produced by using a lathe, and not a by-product of the joining technique. It is perceivable that this will have an effect on the conductivity across the sample, however the contact between the pulled Cu and the bulk CFC is poor therefore thermal conduction will also be poor. Additionally, with the LFA technique the thermal flux from the laser is at its greatest along the central profile of the sample and lowest at the edge and, due to this accounting for a low percentage of the CFC–Cu contact area, it is expected that the effect will be limited. Secondly, of the four samples this one has the largest structures, in height and diameter, protruding from the Cu surface. These structures can be seen to fill pores in the CFC at the interface, however they are not solid Cu, but themselves contain large voids. The pores containing the Cu structures are larger than the characteristic porosity seen in these CFCs. As the CFC is previously well characterised, it is

unlikely that this specific sample had such large pores previous to the joining process. Therefore, it can be inferred that the direct casting process damages the CFC structure by enlarging some already existing porosity. In doing so, the molten Cu fills the newly formed large pores but leaves behind almost equally sized pores in the bulk Cu. In addition to these large protruding Cu structures, small veins of Cu can be seen entering the smaller pores on the CFC surface.

The most notable feature seen in the sample joined by the one step brazing technique is a large void formed as a layer between the bulk Cu and the braze, shown in Fig. 14. This void spans the majority of the surface with the exception of a few ‘pillars’ which connect the upper and lower parts of the sample. On the CFC–Cu interface it can be seen that the braze is present across the greater part of the CFC surface, showing it has successfully bonded. Here it infiltrates the majority of the pores, to a lesser depth than sample DC but deeper than both GG and GS samples. Initially this suggests a superior bond but this is undermined by the large void which suggests substantial delamination between braze and Cu.

Samples GG and GS, joined by the modified braze, shown in Figs. 15 and 16 respectively, show much fewer voids between the bulk Cu and CFC. Additionally, the veins of braze entering the porosity are fewer and less deep. Of the two, sample GS shows the fewest voids in addition to having the fewest and shortest veins protruding from the bulk Cu.

It therefore appears that as the quantity of Cu or braze which enters the CFC porosity increases, so does the volume of voids between the two layers. In the case of DC, this is probably due to the gas which was present in the porosity being forced out as bubbles when the molten Cu is introduced but not able to completely escape. With brazed samples, small voids will inherently be present as part of the layup between layers before the joining process. In joining, it appears these are trapped between layers and locate to the regions where there is the most displacement of braze material i.e. where braze enters the pores. Alternatively, it is possible that as the braze melted and filled the pores, there was insufficient braze material to remain between the CFC and Cu. Due to the brazing process happening at a temperature below the melting point of Cu, the Cu would not then fill the region vacated by the braze thus leaving a void in its place.

Verification of the visual investigation can be made by comparison with the statistical measurements of the data, shown in Table 5. This is done by comparing the surface area of the Cu, calculated as the area of a circle using its diameter, with that measured from the CT data which accounts for surface roughness. To give an indication of joining success, the percentage of this area in contact with the CFC is measured. Quantification of the interlayer voids is also given as percentages of volume and area in the  $x$ – $y$  plane with respect to that of the total volume and planar area of the sample.

Compared to the geometrically calculated surface, all samples have an increased Cu surface area at the interface i.e. none are perfectly smooth. This is due to the deformations introduced in the Cu/braze whilst joining to the CFC. The greatest changes seen are in the DC and GG samples.

It can be seen that both samples with a modified CFC surface (DC and OSB) have a high percentage of the Cu/braze in contact with the CFC, 96.7% and 91.6% respectively, with GG only having 56.3% contact. Therefore, we observe that an increase in Cu surface area does not necessarily lead to a large CFC–Cu contact area. However, recalling the sample thermal conductivities, it must be noted that neither does a high contact area imply higher thermal conductivity e.g. OSB has the second highest contact area ratio but the lowest conductivity by a considerable margin.

This can be attributed to the other major mechanism affecting conductivity across the interface, the existence of voids. A comparison of volume ratio shows that OSB does indeed have a significantly higher volume ratio of porosity. However, GS has

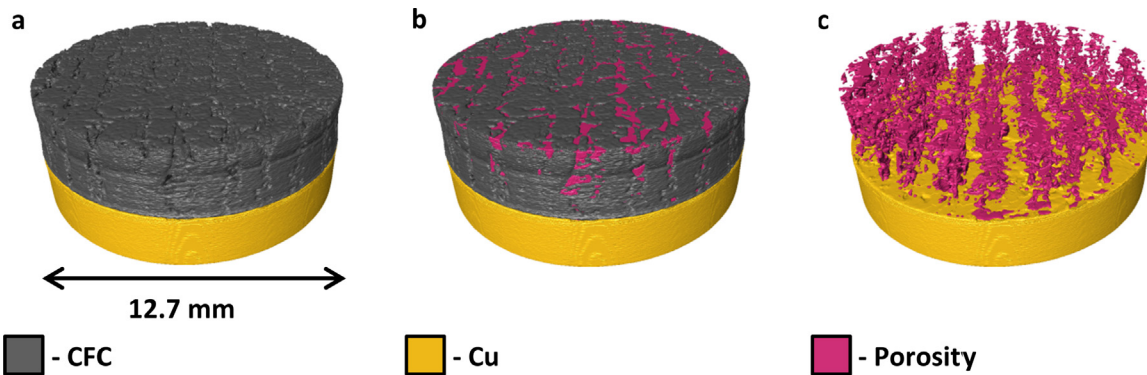


Fig. 12. 3D volumetric rendering of CT data, showing (a) CFC–Cu-GS, (b) same sample with porosity highlighted and (c) CFC removed to display porosity alignment.

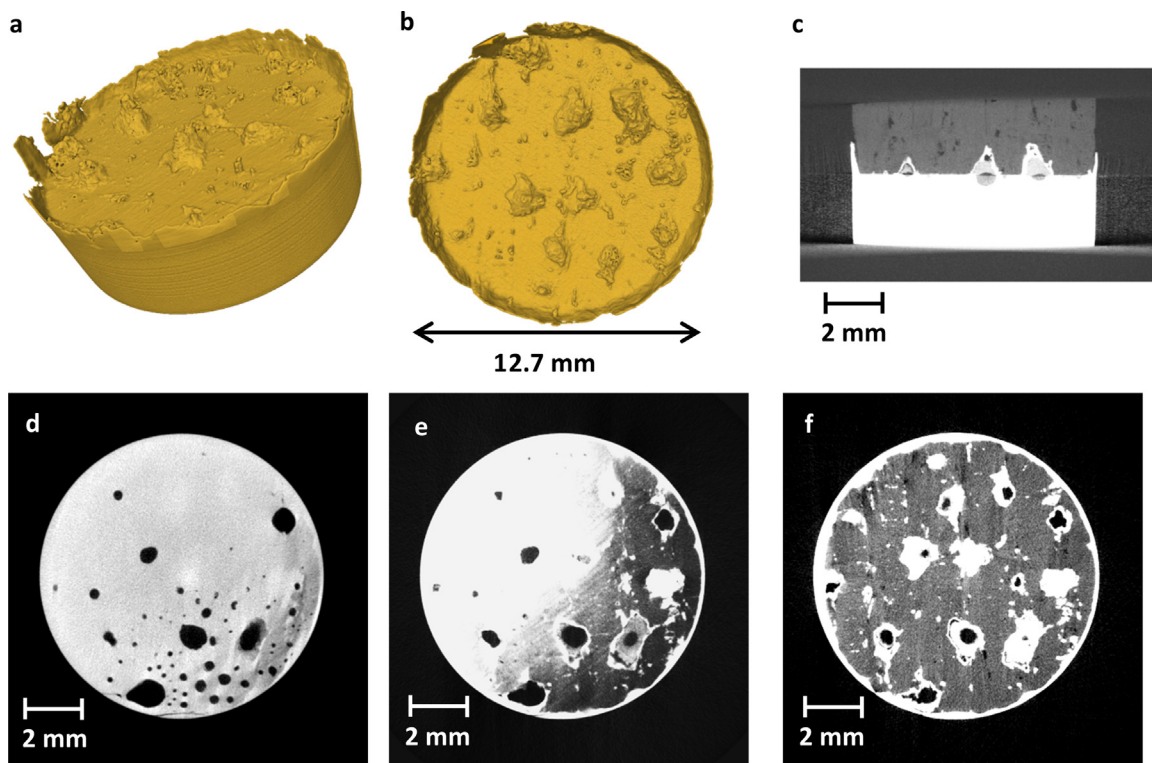


Fig. 13. CT data of CFC–Cu-DC sample represented by; (a), (b) 3D visualisation of Cu showing protruding interface features, (c) tomography slice in  $x$ - $z$  plane showing Cu features (containing voids) entering porosity in CFC, (d), (e) and (f) tomography slices in  $x$ - $y$  plane progressing through the interface from Cu into CFC.

the lowest ratio but not the highest conductivity. It is therefore appropriate to further investigate the voids by considering their shape and distribution.

The thermal pulse from the LFA travels in the  $z$ -direction, therefore features acting as thermal barriers will be most effective in impeding thermal transport by spanning the  $x$ - $y$  plane. Fig. 17 displays the area in that plane covered by the voids (this is given as a percentage of the total sample area in Table 5). By making the

assumption that the voids were perfectly insulating, the lateral area of the voids was used to predict thermal conductivity of the joins, as shown in Eq. (5).

$$K = K_{\text{avg}} \cdot (1 - A_{\text{void}}) \quad (5)$$

where  $K_{\text{avg}}$  is the average thermal conductivity calculated from the constituent material thicknesses as defined in Eq. (4) and  $A_{\text{void}}$  is the lateral area of the sample covered by voids as a fraction.

Table 5

Comparison of Cu area calculated by diameter and measured by CT, also percentage of area in contact with CFC and void volume as percentage of total volume and void area in  $x$ - $y$  plane as percentage of total planar area.

Sample	Cu geometric area ( $\times 10^{-6} \text{ m}^2$ )	Cu CT Area		CFC–Cu contact area (%)	Void volume (% of total vol.)	Void area in $x$ - $y$ (% of total area)
		( $\times 10^{-6} \text{ m}^2$ )	Ratio			
DC	79.80	101.66	1.27	96.7	0.48	10.3
OSB	79.80	87.38	1.09	91.6	2.83	77.2
GG	125.88	154.48	1.23	56.3	0.79	61.2
GS	126.68	132.18	1.04	80.4	0.34	26.7

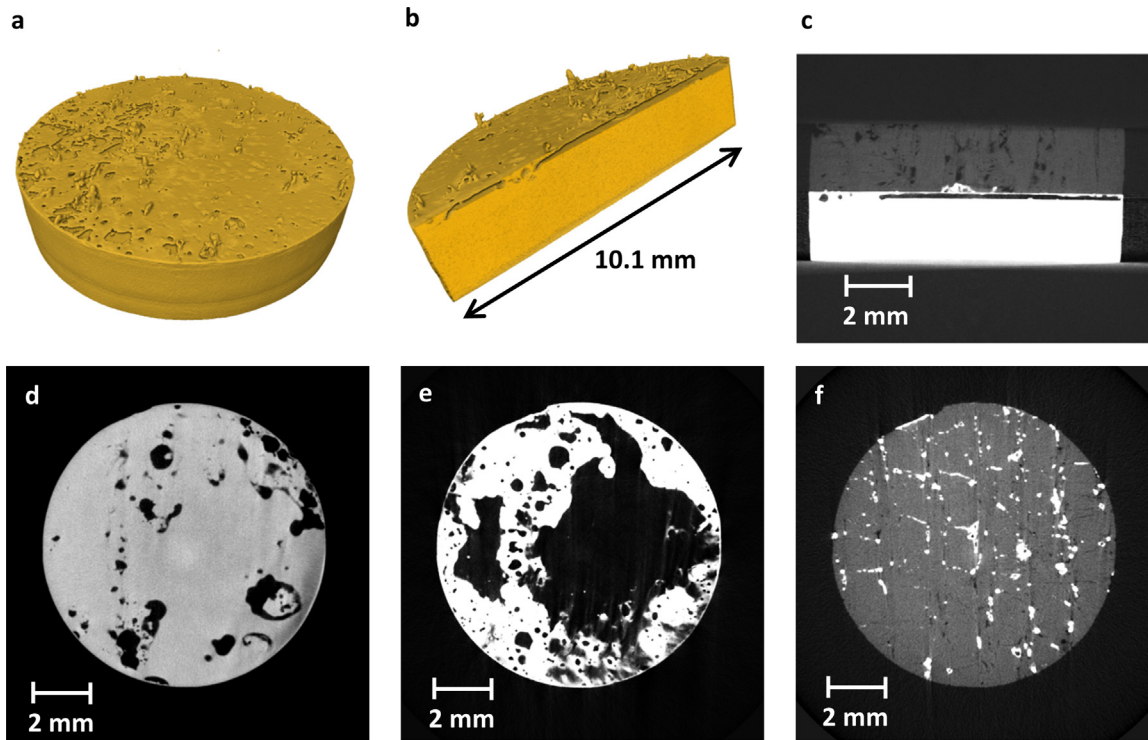


**Fig. 14.** CT data of CFC–Cu.OSB sample represented by: (a), (b) 3D visualisation of Cu showing protruding interface features and void layer between bulk Cu and braze, (c) tomography slice in  $x$ – $z$  plane showing Cu features entering porosity in CFC, (d), (e) and (f) tomography slices in  $x$ – $y$  plane progressing through the interface from Cu into CFC.

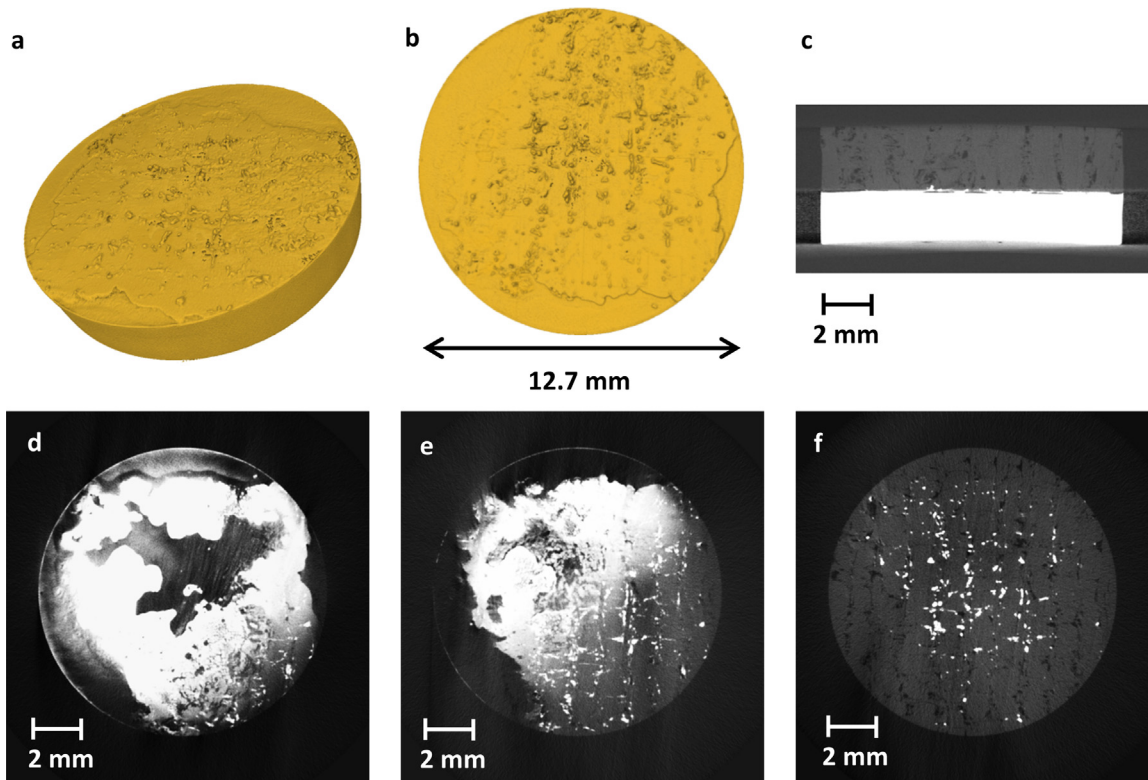


**Fig. 15.** CT data of CFC–Cu.GG sample represented by: (a), (b) 3D visualisation of Cu showing protruding interface features, (c) tomography slice in  $x$ – $z$  plane showing Cu veins of braze entering porosity in CFC, (d–f) tomography slices in  $x$ – $y$  plane progressing through the interface from Cu into CFC.

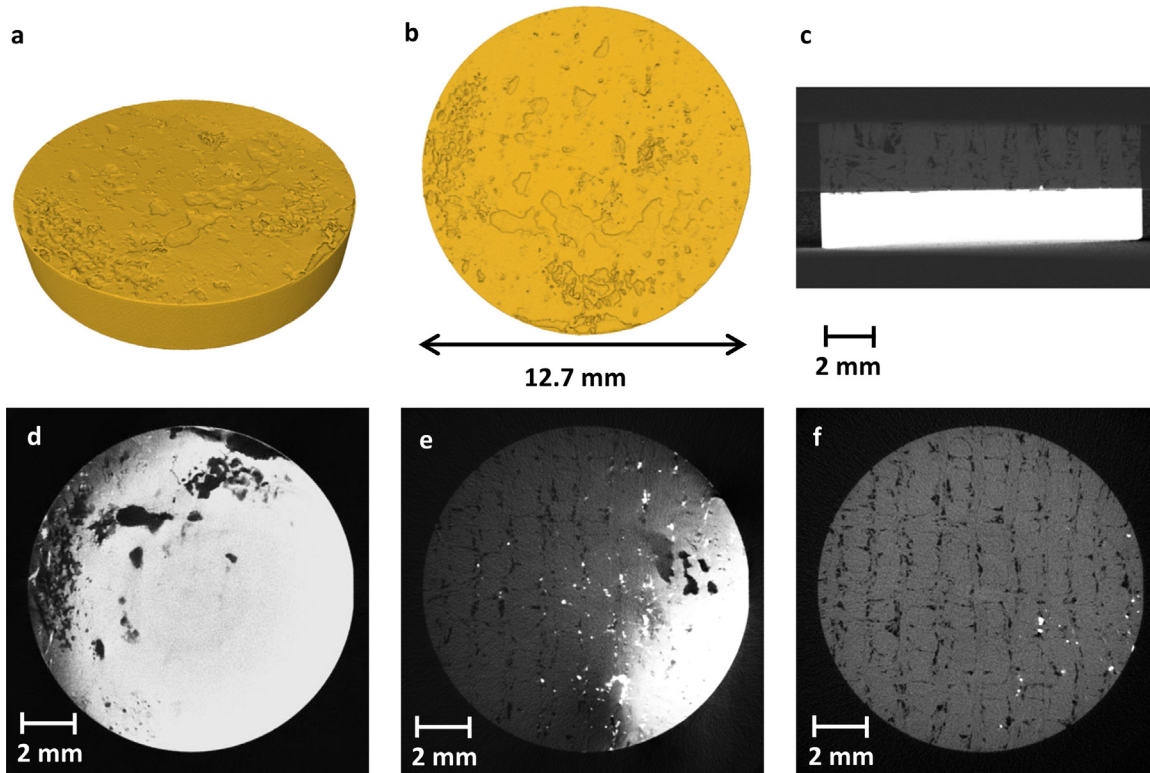


**Fig. 16.** CT data of CFC–Cu.GS sample represented by; (a), (b) 3D visualisation of Cu showing protruding interface features, (c) tomography slice in  $x$ – $z$  plane showing Cu veins of braze entering porosity in CFC, (d–f) tomography slices in  $x$ – $y$  plane progressing through the interface from Cu into CFC.

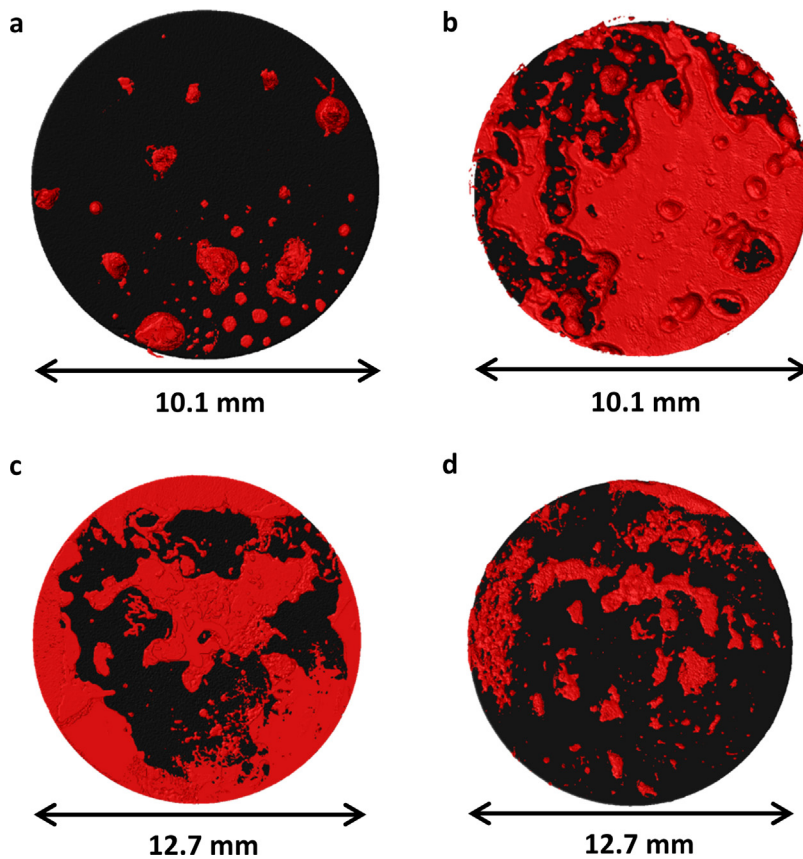


**Fig. 17.** Projection of void area (red) covering total sample area (black) in  $x$ – $y$  plane for samples (a) DC, (b) OSB, (c) GG and (d) GS. (For interpretation of the references to color in this figure legend, the reader is referred to the web version of this article.)

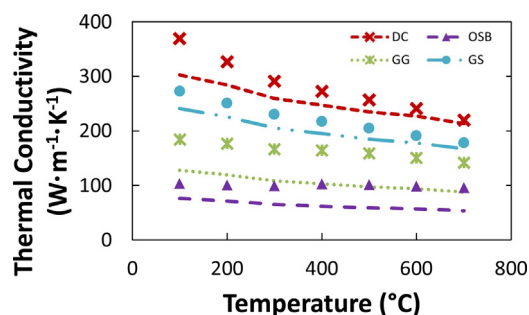


Fig. 18. Thermal conductivity of the four joined samples with points denoting experimental results and lines denoting predicted values based on contribution of constituent material thickness and percentage of sample area covered by voids.

The predicted thermal conductivities are shown along with experimental results for comparison in Fig. 18. The predictions are lower than experimental results because assuming voids are perfectly insulating has artificially increased the thermal resistance. But even with this bold assumption it can be seen that this is a fair approximation of thermal conductivities across the interface. Therefore, when considering samples not easily tested by LFA, quantification of interface voids could provide rough estimates for conductivity. It can be seen that, of the micro-structural features considered, the lateral void area shows the best indication of which samples would be expected to have the highest thermal conductivity.

Although the overall performance across the interface is a combination of the factors discussed, it is implied that the greatest influence on the thermal conductivity comes from the existence of voids between the bulk Cu and CFC and not the CFC–Cu contact area. Therefore to maximise conductivity it is more important to minimise the lateral spread of voids rather than minimise void volume.

Of the samples considered, it was shown that DC had the highest thermal conductivity and lowest lateral void area. This was the only sample not joined by brazing; consequently it is apparent that the brazing technique itself is the cause of the lateral spread in voids observed in the other samples. A possible explanation for this is that too little brazing material was used between the Cu and CFC, therefore leaving these voids when becoming molten and entering the CFC porosity. As a more cost effective alternative, GS shows promise in retaining an adequately comparable thermal conductivity whilst requiring a simpler manufacturing process.

## 5. Conclusions

The thermal performances of four different ceramic/metal joining techniques were investigated by measuring the thermal diffusivity across a CFC–Cu interface. Two samples, joined by direct casting (DC) and a brazing process (OSB), had the CFC modified by applying a coating of chromium to improve its adhesion. The other two used the same brazing process but with the brazing foil pre-coated with chromium. The two methods used for chromium coating were galvanisation (GG) and sputtering (GS). The thermal diffusivities of the joined CFC–Cu samples as well as CFC and Cu only samples were measured by laser flash analysis from 100 °C to 700 °C. Their specific heat capacities were calculated by calibrating results with the reference sample Pyroceram 9606 and thermal conductivities calculated by the combination of these results with their measured densities. Even though samples of similar geometries were tested, each join exhibited a different thermal conductivity across the CFC–Cu interface.

Further investigation of the micro-structures at the CFC–Cu interface was performed by X-ray tomography. Through

quantification of this data a clear link was made between the lateral spread of voids across the interface and thermal conductivity. Recommendations were made to increase thermal conductivity at the CFC–Cu interface by reducing the spread of voids across the interface during the joining process as this was the dominant process in reducing thermal performance.

## Acknowledgements

The support of the Engineering and Physical Sciences Research Council for this work and the Fusion Doctoral Training Network (Grants EP/P504724/1 and EP/H012605/1) and Culham Centre for Fusion Energy (CCFE) is gratefully acknowledged. The authors would like to acknowledge the assistance provided the Manchester X-ray Imaging Facility for use of tomography equipment, which was funded in part by the EPSRC (grants EP/F007906/1, EP/F001452/1 and EP/I02249X/1). Additionally, the authors would like to thank the staff at the University of Manchester, Monica Ferraris (Politecnico di Torino) and David Yapp (CCFE) for guidance in preparing this work, also Dr. G. Pintsuk and Mr. T. Koppitz (Forschungszentrum Jülich, Germany) for manufacturing the GG sample.

## References

- [1] "ITER – the way to new energy." (Online). Available: <http://www.iter.org/proj/itermission> (accessed 25.07.13).
- [2] R. Tivey, T. Ando, A. Antipenkov, V. Barabash, S. Chiochio, G. Federici, et al., ITER divertor, design issues and research and development, *Fusion Eng. Des.* 46 (2–4) (1999) 207–220.
- [3] E. Rigal, P. Bucci, G. Le Marois, Fabrication of monoblock high heat flux components for ITER divertor upper vertical target using hot isostatic pressing diffusion welding, *Fusion Eng. Des.* 49–50 (2000) 317–322.
- [4] M. Missirlian, J. Bucalossi, Y. Corre, F. Ferlay, M. Firdaouss, P. Garin, et al., The WEST project: current status of the ITER-like tungsten divertor, *Fusion Eng. Des.* (2014), <http://dx.doi.org/10.1016/j.fusengdes.2014.01.050>.
- [5] A. Kukushkin, H. Pacher, V. Kotov, G. Pacher, D. Reiter, Finalizing the ITER divertor design: the key role of SOLPS modeling, *Fusion Eng. Des.* 86 (12) (2011) 2865–2873.
- [6] R.A. Pitts, A. Kukushkin, A. Loarte, A. Martin, M. Merola, C. Kessel, Status and physics basis of the ITER divertor, *Phys. Scr.* T138 (2009) 014001.
- [7] T. Hirai, F. Escourbiac, S. Carpentier-Chouchana, A. Fedosov, L. Ferrand, T. Jokinen, et al., ITER tungsten divertor design development and qualification program, *Fusion Eng. Des.* 88 (9–10) (2013) 1798–1801.
- [8] M. Merola, G. Vieider, On the use of flat tile armour in high heat flux components, *J. Nucl. Mater.* 258–263 (Part 1) (1998) 672–676.
- [9] V. Casalegno, M. Salvo, S. Murdaca, M. Ferraris, One-step brazing process for CFC monoblock joints and mechanical testing, *J. Nucl. Mater.* 393 (2) (2009) 300–305.
- [10] B. Schedler, T. Huber, T. Friedrich, E. Eidenberger, M. Kapp, C. Scheu, et al., Characteristics of an optimized active metal cast joint between copper and C/C, *Phys. Scr.* T128 (2007) 200–203.
- [11] P. Appendino, M. Ferraris, V. Casalegno, M. Salvo, M. Merola, Proposal for a new technique to join CFC composites to copper, *J. Nucl. Mater.* 348 (2006) 102–107.
- [12] E. Visca, S. Libera, A. Mancini, G. Mazzone, A. Pizzuto, C. Testani, Hot radial pressing: an alternative technique for the manufacturing of plasma-facing components, *Fusion Eng. Des.* 75–79 (2005) 485–489.
- [13] M. Bisio, V. Branca, M. Di Marco, A. Federici, M. Grattarola, C. Gualco, et al., Manufacturing and testing in reactor relevant conditions of brazed plasma facing components of the ITER divertor, *Fusion Eng. Des.* 75–79 (2005) 277–283.
- [14] M. Salvo, V. Casalegno, S. Rizzo, F. Smeacetto, F. Ferraris, M. Merola, One-step brazing process to join CFC composites to copper and copper alloy, *J. Nucl. Mater.* 374 (2008) 69–74.
- [15] K. Ezato, M. Dairaku, M. Taniguchi, K. Sato, S. Suzuki, M. Akiba, et al., Development of ITER divertor vertical target with annular flow concept – II: development of brazing technique for CFC/CuCrZr joint and heating test of large-scale mock-up, *Fusion Sci. Technol.* 46 (4) (2004) 530–540.
- [16] P. Appendino, M. Ferraris, V. Casalegno, M. Salvo, M. Merola, M. Grattarola, Direct joining of CFC to copper, *J. Nucl. Mater.* 329–333 (Part B) (2004) 1563–1566.
- [17] V. Casalegno, T. Koppitz, G. Pintsuk, M. Salvo, S. Rizzo, S. Perero, et al., Proposal for a new brazing alloy for joining CFC composites to copper, *Compos. B: Eng.* 56 (2014) 882–888.
- [18] O. Abdel Gawad, M.H. Abou Tabl, Z. Abdel Hamid, S.F. Mostafa, Electroplating of chromium and Cr-carbide coating for carbon fiber, *Surf. Coat. Technol.* 201 (3–4) (2006) 1357–1362.
- [19] S. Min, J. Blumm, A. Lindemann, A new laser flash system for measurement of the thermophysical properties, *Thermochim. Acta* 455 (1–2) (2007) 46–49.

- [20] R.D. Cowan, Pulse method of measuring thermal diffusivity at high temperatures, *J. Appl. Phys.* 34 (4) (1963) 926–927.
- [21] W.J. Parker, R.J. Jenkins, C.P. Butler, G.L. Abbott, Flash method of determining thermal diffusivity, heat capacity, and thermal conductivity, *Appl. Phys.* 32 (9) (1961) 1679–1684.
- [22] R. Taylor, J. Jortner, H. Groot, Thermal diffusivity of fiber-reinforced composites using the laser flash technique, *Carbon* 23 (2) (1985) 215–222.
- [23] “ITER Materials Properties Handbook (MPH),” ITER Doc. ITER.D.29DDCW (internal project document distributed to the ITER Participants).
- [24] V. Casalegno, M. Salvo, M. Ferraris, F. Smeacetto, M. Merola, M. Bettuzzi, Non-destructive characterization of carbon fiber composite/Cu joints for nuclear fusion applications, *Fusion Eng. Des.* 83 (5–6) (2008) 702–712.